
High-resolution Simulation of Detonations with Detailed Chemistry

Ralf Deiterding¹ and Georg Bader²

¹ California Institute of Technology, 1200 East California Blvd., Mail-Code 158-79, Pasadena, CA 91125, ralf@cacr.caltech.edu

² Institut für Mathematik, Technische Universität Cottbus, Universitätsplatz 3-4, 03044 Cottbus, bader@math.tu-cottbus.de

Abstract

Numerical simulations can be the key to the thorough understanding of the multi-dimensional nature of transient detonation waves. But the accurate approximation of realistic detonations is extremely demanding, because a wide range of different scales need to be resolved. This paper describes an entire solution strategy for the Euler equations of thermally perfect gas-mixtures with detailed chemical kinetics that is based on a highly adaptive finite volume method for blockstructured Cartesian meshes. Large-scale simulations of unstable detonation structures of hydrogen-oxygen detonations demonstrate the efficiency of the approach in practice.

1 Introduction

Reacting flows have been a topic of on-going research since more than hundred years. The interaction between hydrodynamic flow and chemical kinetics can be extremely complex and even today many phenomena are not very well understood. One of these phenomena is the propagation of detonation waves in gaseous media.

A detonation is a shock-induced combustion wave, which internally consists of a discontinuous hydrodynamic shock wave followed by a smooth region of decaying combustion. The adiabatic compression due to the passage of the shock rises the temperature of the combustible mixture above the ignition limit. The reaction results in an energy release that drives the shock wave forward. In a self-sustaining detonation, shock and reaction zone propagate essentially with an identical speed d_{CJ} that is approximated to good accuracy by the classical Chapman-Jouguet (CJ) theory, cf. [37]. But up to now, no theory exists that describes the internal flow structure satisfactory. The Zel'dovich-von Neumann-Döring (ZND) theory is widely believed to reproduce

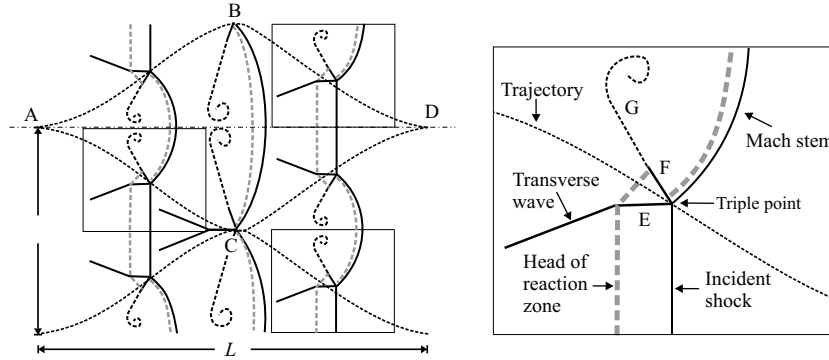


Fig. 1. Left: regular detonation structure at three different time steps on triple point trajectories, right: enlargement of a periodical triple point configuration. E: reflected shock, F: slip line, G: diffusive extension of slip line with flow vertex.

the one-dimensional detonation structure correctly, but already early experiments [7, 30] uncovered that the reduction to one space dimension is not even justified in long combustion devices. It was found that detonation waves usually exhibit non-neglectable instationary multi-dimensional sub-structures and do not remain planar. The multi-dimensional instability manifests itself in instationary shock waves propagating perpendicular to the detonation front. A complex flow pattern is formed around each *triple point*, where the detonation front is intersected by a transverse shock. Pressure and temperature are increased remarkable in a triple point and the chemical reaction is enhanced drastically giving rise to an enormous local energy release. Hence, the accurate representation of triple points is essential for safety analysis, but also in technical applications, e.g. in the pulse detonation engine. Some particular mixtures, e.g. low-pressure hydrogen-oxygen with high argon diluent, are known to produce very regular triple point movements. The triple point trajectories form regular “fish-scale” patterns, so called detonation cells, with a characteristic length L and width λ (compare left sketch of Fig. 1).

Fig. 1 displays the hydrodynamic flow pattern of a detonation with regular cellular structure, how it is known since the early 1970th, cf. [29, 23]. The right sketch shows the periodic wave configuration around a triple point in detail. It consists of a Mach reflection, a flow pattern well-known from non-reactive supersonic hydrodynamics [4]. The undisturbed detonation front is called the incident shock, while the transverse wave takes the role of the reflected shock. The triple point is driven forward by a strong shock wave, called Mach stem. Mach stem and reflected shock enclose the slip line, the contact discontinuity.

The Mach stem is always much stronger than the incident shock, what results in a considerable reduction of the induction length l_{ig} , the distance between leading shock and measurable reaction. The shock front inside the detonation cell travels as two Mach stems from point A to the line BC. In the points B and C the triple point configuration is inverted nearly instan-

taneously and the front in the cell becomes the incident shock. Along the symmetry line AD the change is smooth and the shock strength decreases continuously. In D the two triple points merge exactly in a single point. The incident shock vanishes completely and the slip line, which was necessary for a stable triple point configuration between Mach stem and incident shock, is torn off and remains behind. Two new triple points with two new slip lines develop immediately after D.

But the experimental analysis of the described transient sub-structures is difficult. Direct numerical simulation of the governing equations can be an alternative here [24, 8, 11, 16, 36, 33]. In the following, we will demonstrate that recent parallel computers of moderate size, e.g. clusters of standard personal computers, allow detonation structure simulations in two and three space dimensions even for detailed non-equilibrium chemistry that provide deep insight into the internal flow structure far beyond previous experimental results [29, 23].

2 Detonation Modeling

The governing equations for detonation propagation in premixed gases with realistic chemistry are the Euler equations for multiple thermally perfect species with chemically reactive source terms [10, 37]. In d -dimensional Cartesian coordinates these equations can be written as an inhomogeneous conservation law of the structure

$$\frac{\partial}{\partial t} \mathbf{q}(\mathbf{x}, t) + \sum_{n=1}^d \frac{\partial}{\partial x_n} \mathbf{f}_n(\mathbf{q}(\mathbf{x}, t)) = \mathbf{s}(\mathbf{q}(\mathbf{x}, t)), \quad \mathbf{x} = (x_1, \dots, x_d)^T \in \mathbb{R}^d, \quad t \in \mathbb{R}_0^+, \quad (1)$$

where $\mathbf{q} = \mathbf{q}(\mathbf{x}, t) \in S \subset \mathbb{R}^M$ denotes the vector of conserved quantities. The functions $\mathbf{f}_n(\mathbf{q}) \in C^1(S, \mathbb{R}^M)$, $n = 1, \dots, d$ are the hydrodynamic fluxes, $\mathbf{s}(\mathbf{q}) \in C^1(S, \mathbb{R}^M)$ is the source term.

2.1 Euler Equations for Gas-Mixtures

For the multi-component Euler equations with K species the vector of conserved quantities has $M = K + d + 1$ components. We choose the form

$$\mathbf{q}(\mathbf{x}, t) = (\rho_1, \dots, \rho_K, \rho u_1, \dots, \rho u_d, \rho E)^T. \quad (2)$$

The partial density of the i th species is denoted by ρ_i , where $i = 1, \dots, K$. The total density of the mixture $\rho = \sum_{i=1}^K \rho_i$ is a conserved quantity, too. The ratios $Y_i = \rho_i / \rho$ are called mass fractions. They satisfy the relation $\sum_{i=1}^K Y_i = 1$. We denote the n th component of the velocity vector $\mathbf{u} = (u_1, \dots, u_d)^T$ by u_n and E is the total energy per unit mass. The flux functions are

$$\mathbf{f}_n(\mathbf{q}) = (\rho_1 u_n, \dots, \rho_K u_n, \rho u_1 u_n + \delta_{1n} p, \dots, \rho u_d u_n + \delta_{dn} p, u_n(\rho E + p))^T \quad (3)$$

for $n = 1, \dots, d$. Herein, p is the hydrostatic pressure and δ_{jn} denotes the Kronecker-Symbol. We assume that all species are ideal gases in thermal equilibrium. Under this assumption the same temperature T can be used to evaluate the partial pressure of all species as $p_i = \mathcal{R}T\rho_i/W_i$ with \mathcal{R} denoting the universal constant and W_i the molecular weight, respectively. According to Dalton's law the total pressure is given by

$$p = \sum_{i=1}^K p_i = \mathcal{R}T \sum_{i=1}^K \frac{\rho_i}{W_i}. \quad (4)$$

Each species is assumed to be *thermally perfect* and has a temperature-dependent specific heat $c_{pi}(T)$. The functions $c_{pi}(T)$ are usually approximated by polynomials of degree 4 which are valid within a restricted temperature range, e.g. from 300 K to 5000 K [31, 20]. The enthalpies per unit mass are written as

$$h_i(T) = h_i^0 + \int_{T^0}^T c_{pi}(\sigma) d\sigma$$

with h_i^0 called the heat of formation at the reference temperature T^0 . For the enthalpy of the mixture $h = \sum_{i=1}^K Y_i h_i(T)$ holds true. Inserting this into the thermodynamic relation $\rho h - \rho E + \rho \mathbf{u}^2/2 - p = 0$ and inserting Eq. (4) for p yields

$$\varphi(\mathbf{q}, T) := \sum_{i=1}^K \rho_i h_i(T) - \rho E + \rho \frac{\mathbf{u}^2}{2} - \mathcal{R}T \sum_{i=1}^K \frac{\rho_i}{W_i} = 0. \quad (5)$$

It can be proven rigorously [5], that for each \mathbf{q} in the space of admissible states S a unique temperature T exists that satisfies Eq. (5). Unfortunately, a closed form of the inverse can only be derived under simplifying assumptions and the computation of T from Eq. (5) is in general unavoidable, whenever the pressure p has to be evaluated. The appropriate speed of sound for the described model is the *frozen* speed of sound, which is given by

$$c^2 = \left(\frac{\partial p}{\partial \rho} \right)_{s, Y_1, \dots, Y_K} = \sum_{i=1}^K Y_i \phi_i - (\gamma - 1) (\mathbf{u}^2 - H) \quad (6)$$

with $H = h + \frac{\mathbf{u}^2}{2}$ and $\phi_i := \frac{\partial p}{\partial \rho_i} = (\gamma - 1) \left(\frac{\mathbf{u}^2}{2} - h_i(T) \right) + \gamma \frac{\mathcal{R}}{W_i} T$. The coefficient $\gamma = \gamma(Y_1, \dots, Y_K, T)$ can be calculated from the mixture quantities $c_p = \sum_{i=1}^K Y_i c_{pi}(T)$ and $W = \left(\sum_{i=1}^K Y_i/W_i \right)^{-1}$ by employing the relation $\gamma = c_p(c_p - \mathcal{R}/W)^{-1}$. By inserting the previous expression for ϕ_i into Eq. (6) and by applying the ideal-gas law (4) it can be shown, that the frozen speed of sound of a thermally perfect gas-mixture satisfies the relation $c^2 = \gamma p/\rho$.

Mathematical Properties

The Euler equations for thermally perfect gas-mixtures inherit most mathematical properties of the standard Euler equations for a single polytropic gas with equation of state $p = (\gamma - 1)(\rho E - \rho \mathbf{u}^2/2)$, cf. [28]. Utilizing expression (6) for the speed of sound the hyperbolicity of Eq. (1) with vector of state (2) and flux functions (3) can easily be proven [5]. For $d = 2, 3$ the proof uses the validity of the rotational invariance property that carries over from the standard Euler equations almost directly [32] and requires just the diagonalization of the Jacobian $\mathbf{A}_1(\mathbf{q}) = \partial \mathbf{f}_1(\mathbf{q})/\partial \mathbf{q}$. For instance, in two space dimensions the matrix of right eigenvectors $\mathbf{R}_1(\mathbf{q}) = (\mathbf{r}_1 | \dots | \mathbf{r}_{K+d+1})$ that diagonalizes $\mathbf{A}_1(\mathbf{q})$ with $\mathbf{R}_1^{-1}(\mathbf{q}) \mathbf{A}_1(\mathbf{q}) \mathbf{R}_1(\mathbf{q}) = \mathbf{\Lambda}_1(\mathbf{q})$ for all $\mathbf{q} \in S$ with $\mathbf{\Lambda}_1(\mathbf{q}) = \text{diag}(u_1 - c, u_1, \dots, u_1, u_1 + c)$ takes the form

$$\mathbf{R}_1(\mathbf{q}) = \begin{bmatrix} Y_1 & 1 & 0 \dots & 0 & 0 & Y_1 \\ & 0 & & & & \\ \vdots & \vdots & \ddots & \vdots & \vdots & \vdots \\ Y_K & 0 & \dots & 0 & 1 & 0 & Y_K \\ u_1 - c & u_1 & \dots & & u_1 & 0 & u_1 + c \\ u_2 & u_2 & \dots & & u_2 & 1 & u_2 \\ H - u_1 c & \mathbf{u}^2 - \frac{\phi_1}{\gamma - 1} & \dots & \mathbf{u}^2 - \frac{\phi_K}{\gamma - 1} & u_2 & H + u_1 c \end{bmatrix}. \quad (7)$$

Furthermore, it can be shown that the flux functions $\mathbf{f}_n(\mathbf{q})$ and their Jacobians $\mathbf{A}_n(\mathbf{q})$ satisfy the homogeneity property $\mathbf{f}_n(\mathbf{q}) = \mathbf{A}_n(\mathbf{q})\mathbf{q}$ for all $\mathbf{q} \in S$.

The Homogeneous Riemann Problem

The profound understanding of the Riemann Problem (RP) in the non-reactive case provides the theoretical basis for the construction of a reliable Godunov-type method in Sec. 3.2 as a key ingredient for detonation simulation. For $\mathbf{s} \equiv \mathbf{0}$ the solution structure of a quasi-one-dimensional RP with discontinuous initial data

$$\mathbf{q}(\mathbf{x}, 0) = \begin{cases} \mathbf{q}_l, & x_n < 0 \\ \mathbf{q}_r, & x_n > 0 \end{cases}, \quad (8)$$

can be shown to be in principle identical to the standard case of a single polytropic gas that is discussed in detail for example in [28, 12, 32]. The first and last characteristic field with the eigenvalues $u_n - c$ and $u_n + c$ are genuinely nonlinear, provided that the condition

$$\frac{\gamma(\gamma + 1)}{(1 - \gamma)T} \neq \frac{\partial \gamma}{\partial T} \quad (9)$$

is satisfied for all $\mathbf{q} \in S$ [5]. All other characteristic fields are associated to the eigenvalue u_n and are linearly degenerate. If we *assume* that condition (9) is satisfied, it can be concluded that the solution of the RP consists of admissible shocks or smooth rarefaction waves in the first and last characteristic field, while the contributions in all other characteristic fields sum up to a single contact discontinuity.

Unlike standard Euler equations, no complete set of Riemann invariants can be found for the Euler equations for thermally perfect gases [22]. The only Riemann invariants that can be derived are the mass fractions Y_i , which are constant across the first and last characteristic field [5], and the velocity u_n and the pressure p , which are invariant across the contact discontinuity.

2.2 Reactive Source Terms

We write the source term of detailed chemical reaction in the form

$$\mathbf{s}(\mathbf{q}) = (W_1 \dot{\omega}_1, \dots, W_K \dot{\omega}_K, 0, \dots, 0, 0)^T .$$

The chemical production of each species is expressed as product of its production rate in molar concentration per unit volume $\dot{\omega}_i = \dot{\omega}_i(\mathbf{q}) \in C^1(S, \mathbb{R})$ and W_i . The rates $\dot{\omega}_i(\rho_1, \dots, \rho_K, T)$ are derived from a reaction mechanism of J chemical reactions

$$\sum_{i=1}^K \nu_{ji}^f S_i \rightleftharpoons \sum_{i=1}^K \nu_{ji}^r S_i, \quad j = 1, \dots, J,$$

where ν_{ji}^f and ν_{ji}^r are the stoichiometric coefficients of species S_i appearing as a reactant and as a product. The entire molar production rate of species S_i per unit volume is then given by

$$\dot{\omega}_i = \sum_{j=1}^J (\nu_{ji}^r - \nu_{ji}^f) \left[k_j^f \prod_{l=1}^K \left(\frac{\rho_l}{W_l} \right)^{\nu_{jl}^f} - k_j^r \prod_{l=1}^K \left(\frac{\rho_l}{W_l} \right)^{\nu_{jl}^r} \right], \quad i = 1, \dots, K, \quad (10)$$

with $k_j^f(T)$ and $k_j^r(T)$ denoting the forward and backward reaction rate of each chemical reaction [37]. The reaction rates are calculated by the Arrhenius law

$$k_j^{f/r}(T) = A_j^{f/r} T^{\beta_j^{f/r}} \exp(-E_j^{f/r}/\mathcal{R}T). \quad (11)$$

Some backward reaction rates might be derived by assuming the corresponding chemical reaction to be in chemical equilibrium, but especially detonations usually require mechanisms that utilize non-equilibrium backward reaction rates at least for some of the reactions. A chemical kinetics package, e.g. Chemkin [19], can be utilized to evaluate (10), (11) according to the reaction mechanism and given thermodynamic data.

3 Numerical Methods

We use the time-operator splitting approach or method of fractional steps [17] to decouple hydrodynamic transport and chemical reaction numerically. This technique is most frequently used for time-dependent reactive flow computations. The homogeneous partial differential equation

$$\mathcal{H}^{(\Delta t)} : \frac{\partial \mathbf{q}}{\partial t} + \sum_{n=1}^d \frac{\partial}{\partial x_n} \mathbf{f}_n(\mathbf{q}) = 0, \quad \text{IC: } \mathbf{Q}^\kappa \xrightarrow{\Delta t} \tilde{\mathbf{Q}}^{\kappa+1} \quad (12)$$

and the usually stiff ordinary differential equation

$$\mathcal{S}^{(\Delta t)} : \frac{\partial \mathbf{q}}{\partial t} = \mathbf{s}(\mathbf{q}), \quad \text{IC: } \tilde{\mathbf{Q}}^{\kappa+1} \xrightarrow{\Delta t} \mathbf{Q}^{\kappa+1} \quad (13)$$

are integrated successively with the data \mathbf{Q} from the preceding step as initial condition (IC).

3.1 Finite Volume Schemes

The appropriate discretization technique for conservation laws with discontinuous solution is the finite volume (FV) approach. For simplicity, we assume an equidistant discretization in two space dimensions with mesh widths Δx_1 , Δx_2 and a constant time step Δt . A conservative time-explicit finite volume scheme for Eq. (12) has the formal structure

$$\mathcal{H}^{(\Delta t)} : \tilde{\mathbf{Q}}_{jk}^{\kappa+1} = \mathbf{Q}_{jk}^\kappa - \frac{\Delta t}{\Delta x_1} \left[\mathbf{F}_{j+\frac{1}{2},k}^1 - \mathbf{F}_{j-\frac{1}{2},k}^1 \right] - \frac{\Delta t}{\Delta x_2} \left[\mathbf{F}_{j,k+\frac{1}{2}}^2 - \mathbf{F}_{j,k-\frac{1}{2}}^2 \right] \quad (14)$$

and satisfies the important discrete conservation property $\sum_{j,k} \tilde{\mathbf{Q}}_{jk}^{\kappa+1} = \sum_{j,k} \mathbf{Q}_{jk}^\kappa$ for vanishing boundary fluxes. Such a scheme can easily be constructed by applying the idea of operator splitting also to Eq. (12) and by using two quasi-one-dimensional FV schemes successively, e.g.

$$\tilde{\mathbf{Q}}_{jk}^{\kappa+\frac{1}{2}} = \mathbf{Q}_{jk}^\kappa - \frac{\Delta t}{\Delta x_1} \left[\mathbf{F}^1(\mathbf{Q}_{j-\nu+1,k}^\kappa, \dots, \mathbf{Q}_{j+\nu,k}^\kappa) - \mathbf{F}^1(\mathbf{Q}_{j-\nu,k}^\kappa, \dots, \mathbf{Q}_{j+\nu-1,k}^\kappa) \right],$$

$$\tilde{\mathbf{Q}}_{jk}^{\kappa+1} = \tilde{\mathbf{Q}}_{jk}^{\kappa+\frac{1}{2}} - \frac{\Delta t}{\Delta x_2} \left[\mathbf{F}^2(\tilde{\mathbf{Q}}_{j,k-\nu+1}^{\kappa+\frac{1}{2}}, \dots, \tilde{\mathbf{Q}}_{j,k+\nu}^{\kappa+\frac{1}{2}}) - \mathbf{F}^2(\tilde{\mathbf{Q}}_{j,k-\nu}^{\kappa+\frac{1}{2}}, \dots, \tilde{\mathbf{Q}}_{j,k+\nu-1}^{\kappa+\frac{1}{2}}) \right],$$

i.e. $\mathcal{H}^{(\Delta t)} = \mathcal{X}_2^{(\Delta t)} \mathcal{X}_1^{(\Delta t)}$. With this definition the entire splitting method reads $\mathbf{Q}^{\kappa+1} = \mathcal{S}^{(\Delta t)} \mathcal{X}_2^{(\Delta t)} \mathcal{X}_1^{(\Delta t)}(\mathbf{Q}^\kappa)$. The later method is formally only first-order accurate, but it usually gives very satisfactory results, if high-resolution shock-capturing schemes are employed for the operators $\mathcal{X}_n^{(\Delta t)}$. Formally second-order accurate splitting methods are possible [32], but they lead to similar results in most practical cases and we have observed only minor improvements for typical detonation structure simulations [5]. For the upwind method

formulated in Algorithm 1, the described splitting is stable under the Courant-Friedrichs-Levy (CFL) condition

$$C_{CFL} := \max_{j,k} \left(S_{j+\frac{1}{2},k} \frac{\Delta t}{\Delta x_1}, S_{j,k+\frac{1}{2}} \frac{\Delta t}{\Delta x_2} \right) \leq 1, \quad (15)$$

where $S_{j+\frac{1}{2},k}$, $S_{j,k+\frac{1}{2}}$ denote the maximal signal speeds in both space directions according to step (S12) in Algorithm 1.

3.2 High-resolution Upwind Method

The operators $\mathcal{X}_n^{(\Delta t)}$ can be implemented effectively with a single quasi-one-dimensional scheme that allows the canonical exchange of the velocities u_n and the indices j and k . The method should achieve a higher order of accuracy in smooth solution regions and should approximate discontinuities on the basis of the characteristic information (upwinding) without spurious overshoots. Today, several excellent textbooks are available, e.g. [32], which discuss the construction of quasi-one-dimensional *high-resolution* methods for supersonic hydrodynamics in great detail and we therefore sketch the basic components of our particular method only briefly.

Our high-resolution scheme is built around a first-order Godunov-type method that solves the Riemann problem between two neighboring cell values \mathbf{Q}_l and \mathbf{Q}_r approximately, which we describe exemplary for the x_1 -direction. The method is based on an extension of Roe's linearized Riemann solver for Euler equations for a single polytropic gas for multiple thermally perfect species by Grossman and Cinella [13] that corresponds to the steps (S1) to (S7) in Algorithm 1. The structure of the Roe-averaged right eigenvectors $\hat{\mathbf{r}}_m$ is given in Eq. (7). In (S8), (S9) the two intermediate states of the linearized RP are evaluated and the intrinsic problem of unphysical total densities and internal energies near vacuum due to the Roe linearization, cf. [9], is circumvented by switching in case of an unphysical approximation to the simple, but extremely robust Harten-Lax-Van Leer (HLL) Riemann solver. If Roe's flux approximation is applied in step (S10), violations of the entropy condition are generally avoided by adding an appropriate amount of numerical viscosity [15]. A natural choice for the parameter η for Euler equations is $\eta = \frac{1}{2}(|u_{1,r} - u_{1,l}| + |c_r - c_l|)$, cf. [27].

In one space-dimension, Eq. (16) need only be applied to $\iota = 1, 3$ and $\bar{s}_2 = s_2$ can be used, but two- and three-dimensional detonation simulations usually require the extension of Eq. (16) to $\iota = 2$. The shock of typical detonation waves is extraordinarily strong and its approximation is often corrupted by the carbuncle phenomenon, a multi-dimensional numerical crossflow instability that occurs at strong grid-aligned shocks or detonation waves [26]. The carbuncle phenomenon can

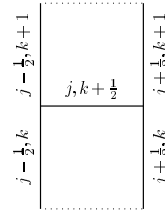


Fig. 2. H-correction between the cells (j, k) and $(j, k + 1)$.

- (S1) Calculate $\hat{\rho} := \sqrt{\rho_l \rho_r}$ and $\hat{v} := \frac{\sqrt{\rho_l} v_l + \sqrt{\rho_r} v_r}{\sqrt{\rho_l} + \sqrt{\rho_r}}$ for u_n, Y_i, H, h_i, T .
- (S2) Compute $\hat{\gamma} := \hat{c}_p / \hat{c}_v$ with $\hat{c}_{\{p/v\}} = \sum_{i=1}^K \hat{Y}_i \hat{c}_{\{p/v\}i}$ and

$$\hat{c}_{\{p/v\}i} = \frac{1}{T_r - T_l} \int_{T_l}^{T_r} c_{\{p,v\}i}(\tau) d\tau.$$
- (S3) Calculate $\hat{\phi}_i := (\hat{\gamma} - 1) \left(\frac{\hat{u}^2}{2} - \hat{h}_i \right) + \hat{\gamma} \frac{\mathcal{R}}{\hat{W}_i} \hat{T}$.
- (S4) Calculate $\hat{c} := \left(\sum_{i=1}^K \hat{Y}_i \hat{\phi}_i - (\hat{\gamma} - 1) (\hat{u}^2 - \hat{H}) \right)^{1/2}$.
- (S5) Use $\Delta \mathbf{Q} = \mathbf{Q}_r - \mathbf{Q}_l$ and Δp to compute the wave strengths

$$a_{1,K+d+1} = \frac{\Delta p \mp \hat{\rho} \hat{c} \Delta u_1}{2 \hat{c}^2}, \quad a_{1+i} = \Delta \rho_i - \hat{Y}_i \frac{\Delta p}{\hat{c}^2}, \quad a_{K+n} = \hat{\rho} \Delta u_n.$$
- (S6) Calculate $\mathbf{W}_1 = a_1 \hat{\mathbf{r}}_1$, $\mathbf{W}_2 = \sum_{m=2}^{K+d} a_m \hat{\mathbf{r}}_m$, $\mathbf{W}_3 = a_{K+d+1} \hat{\mathbf{r}}_{K+d+1}$.
- (S7) Evaluate $s_1 = \hat{u}_1 - \hat{c}$, $s_2 = \hat{u}_1$, $s_3 = \hat{u}_1 + \hat{c}$.
- (S8) Evaluate $\rho_{l/r}^*$, $u_{1,l/r}^*$, $e_{l/r}^*$, $c_{1,l/r}^*$ from $\mathbf{Q}_l^* = \mathbf{Q}_l + \mathbf{W}_1$ and $\mathbf{Q}_r^* = \mathbf{Q}_r - \mathbf{W}_3$.
- (S9) If $\rho_{l/r}^* \leq 0$ or $e_{l/r}^* \leq 0$ set $s_1 = \min(u_{1,l} - c_l, u_{1,r} - c_r)$,
 $s_3 = \max(u_{1,l} + c_l, u_{1,r} + c_r)$, use HLL flux

$$\mathbf{F}(\mathbf{Q}_l, \mathbf{Q}_r) = \begin{cases} \mathbf{f}(\mathbf{Q}_l), & 0 < s_1, \\ \frac{s_3 \mathbf{f}(\mathbf{Q}_l) - s_1 \mathbf{f}(\mathbf{Q}_r) + s_1 s_3 (\mathbf{Q}_r - \mathbf{Q}_l)}{s_3 - s_1}, & s_1 \leq 0 \leq s_3, \\ \mathbf{f}(\mathbf{Q}_r), & 0 > s_3, \end{cases}$$

and go to (S12).

- (S10) Evaluate Roe flux $\mathbf{F}(\mathbf{Q}_l, \mathbf{Q}_r) = \frac{1}{2} (\mathbf{f}(\mathbf{Q}_l) + \mathbf{f}(\mathbf{Q}_r)) - \sum_{i=1}^3 |\tilde{s}_i| \mathbf{W}_i$ with entropy enforcement formula

$$|\tilde{s}_i| = \begin{cases} |s_i|, & |s_i| \geq 2\eta, \\ |s_i|^2 / (4\eta) + \eta, & |s_i| < 2\eta. \end{cases} \quad (16)$$

- (S11) With $\mathbf{F}_\rho := \sum_{i=1}^K \mathbf{F}_i$ replace \mathbf{F}_i by $\mathbf{F}_i^* = \mathbf{F}_\rho \cdot \begin{cases} Y_i^l, & \mathbf{F}_\rho \geq 0, \\ Y_i^r, & \mathbf{F}_\rho < 0. \end{cases}$
- (S12) Evaluate maximal signal speed by $S = \max(|s_1|, |s_3|)$.

Algorithm 1. Hybrid Roe-HLL scheme for detonation simulation.

be avoided completely by applying Eq. (16) to all characteristic fields and evaluating η in a multi-dimensional way. In all computations of Sec. 5 we have successfully utilized the ‘‘H-correction’’ of Sanders et al. [27] for this purpose. For instance in the x_2 -direction it takes the form

$$\tilde{\eta}_{j,k+\frac{1}{2}} = \max \left\{ \eta_{j+\frac{1}{2},k}, \eta_{j-\frac{1}{2},k}, \eta_{j,k+\frac{1}{2}}, \eta_{j-\frac{1}{2},k+1}, \eta_{j+\frac{1}{2},k+1} \right\}$$

in the two-dimensional case, see Fig. 2. Step (S11) ensures the positivity of the mass fractions Y_i , if the Roe approximation is applied [21]. The HLL scheme can be proven to be positivity preserving in Y_i and does not require this step.

A detailed derivation of the entire Roe-HLL scheme and thorough numerical comparisons with various standard methods can be found in [5].

The hybrid Riemann solver is extended to a high-resolution method with the MUSCL-Hancock variable extrapolation technique by Van Leer [34]. The technique uses a five-point stencil with $\nu = 2$. In contrast to the Euler equations for a single polytropic gas, the extrapolation for the Euler equations of Sec. 2.1 can not be formulated completely in conservative variables, because the solvability of the nonlinear equation (5) can not be guaranteed for an extrapolated vector of state. We recommend to apply the MUSCL extrapolation to ρ , p , Y_i and ρu_n and to derive a thermodynamically consistent extrapolated vector of state from these. See [5] for details.

3.3 Integration of Reaction Terms

The numerical treatment of chemical reaction terms with the method of fractional steps requires the solution of the ODE

$$\frac{\partial \rho_i}{\partial t} = W_i \dot{\omega}_i(\rho_1, \dots, \rho_K, T), \quad i = 1, \dots, K$$

with initial condition $\rho_i(0) = \rho Y_i^0$, $i = 1, \dots, K$ in every FV cell. The total density ρ in this cell, the specific energy E and the velocities u_n remain unchanged during the integration, what corresponds to a reaction in an adiabatic constant volume environment. ODEs arising from chemical kinetics are usually stiff and we employ a semi-implicit Rosenbrock-Wanner method by Kaps and Rentrop of fourth order with automatic step-size adjustment [18]. The computational expensive reaction rate expressions (10) are evaluated by a mechanism-specific routine, which is produced by a source code generator on top of the Chemkin-II library [19] in advance. The code generator implements the formulas of Sec. 2.2 without any loops and inserts the constants $\nu_j^{f/r}$, $A_j^{f/r}$, $-E_j^{f/r}$ directly into the code.

3.4 Evaluation of the Temperature

The FV method for thermally perfect gas-mixtures sketched in Sec. 3.2 and the reaction term integration described in Sec. 3.3 require the computation of the temperature T from a discrete vector of state \mathbf{Q} by solving Eq. (5). As Eq. (5) has a unique temperature solution for all admissible vectors of state and $\varphi(\cdot, T)$ can be shown to be a strict monotone function in T (see [5]), the efficient solution of Eq. (5) is straight-forward: We start the solution procedure with a standard Newton iteration that is initialized with the temperature value of the preceding time step. If the Newton method does not converge in a reasonable number of steps, a standard bisection technique is employed.

In order to speed up further the polynomial evaluation of the temperature-dependent properties $c_{pi}(T)$ and $h_i(T)$, look-up tables for all species are constructed during the startup of the computational code. These tables store

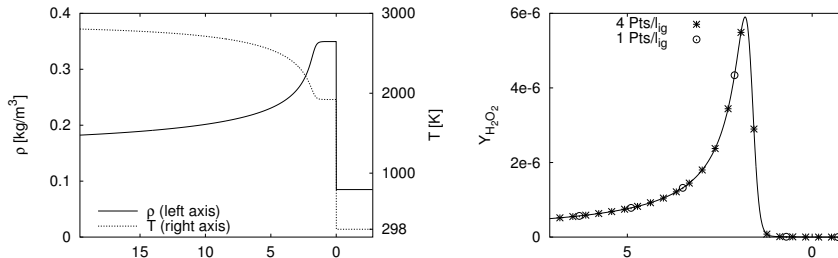


Fig. 3. ZND solution for a self-sustaining hydrogen-oxygen detonation ($d_{CJ} \approx 1627$ m/s, $l_{ig} \approx 1.404$ mm) and representation of the mass fraction of H_2O_2 on different meshes (right). The points represent the value in the center of a finite volume. The abscissas display the distance behind the detonation front in mm.

$c_{pi}(T)$ and $h_i(T)$ for all integers in the valid temperature range and intermediate values are interpolated.

3.5 Meshes for Detonation Simulation

Numerical simulations of detonation waves require computational meshes, which are able to represent the strong local flow changes due to the reaction correctly. In particular, the shock of a detonation wave with detailed kinetics can be very sensitive to changes of the reaction behind and, if the mesh is too coarse to resolve all reaction details correctly, the Riemann Problem at the detonation front is changed remarkably leading to a wrong speed of propagation. We make a simple discretization test in order to illustrate, how fine computational meshes for accurate detonation simulations in fact have to be. The left graph of Fig. 3 displays the flow fields of ρ and T according to the ZND detonation model for the frequently studied $\text{H}_2 : \text{O}_2 : \text{Ar}$ CJ detonation with molar ratios $2 : 1 : 7$ at $T_0 = 298$ K and $p_0 = 6.67$ kPa for a hydrogen-oxygen reaction mechanism extracted from a larger hydrocarbon mechanism assembled by Westbrook [35]. The mechanism uses 34 elementary reactions for the 9 species H, O, OH, H_2 , O_2 , H_2O , HO_2 , H_2O_2 and Ar. Throughout this paper only this mechanism has been employed.

The right graph of Fig. 3 displays the *exact* distribution of $Y_{\text{H}_2\text{O}_2}$ discretized with different FV grids. Even a resolution of 4 finite volumes per induction length ($4 \text{ Pts}/l_{ig}$) is not sufficient to capture the maximum of the intermediate product H_2O_2 correctly. This requires at least 5 to 6 Pts/l_{ig} , but in triple points even finer resolutions are required. The discretization of typical combustors with such fine uniform grids can easily exceed 10^9 FV cells in the two- and 10^{12} cells in the three-dimensional case. As multi-dimensional detonations are intrinsically unstable (compare Sec. 1), numerical simulations have to be instationary and usually involve several ten thousand time steps. Consequently, uniform meshes are far too expensive and the application of a sophisticated dynamically adaptive mesh refinement technique is indispensable.

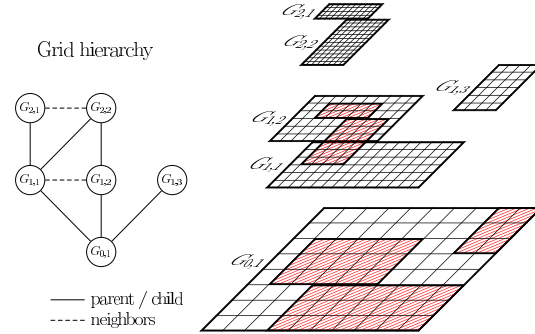


Fig. 4. The AMR method creates a hierarchy of rectangular subgrids.

4 Adaptive Mesh Refinement

In order to supply the required temporal and spatial resolution efficiently, we employ the blockstructured adaptive mesh refinement (AMR) method after Berger and Colella [2, 3] which is tailored especially for hyperbolic conservation laws on logically rectangular FV grids (not necessarily Cartesian). We have implemented the AMR method in a generic, dimension-independent object-oriented framework in C++. It is called AMROC (Adaptive Mesh Refinement in Object-oriented C++) and is free of charge for scientific use [6]. The adaptive algorithm has been realized completely decoupled from a particular FV method. All what the algorithm requires are specific implementations of the operators $\mathcal{H}^{(\cdot)}$ and $\mathcal{S}^{(\cdot)}$ on a single rectangular grid G , where $\mathcal{H}^{(\cdot)}$ has to utilize ν auxiliary cells (ghost or halo cells) around G to define discrete boundary conditions. The entire framework has been validated extensively on a large number of hydrodynamic standard test cases. See [5] and [6] for results.

4.1 Berger-Colella AMR Method

Instead of replacing single cells by finer ones, as it is done in cell-oriented refinement techniques, the Berger-Colella AMR method follows a patch-oriented approach. Cells being flagged by various error indicators (shaded in Fig. 4) are clustered with a special algorithm [1] into non-overlapping rectangular grids $G_{l,m}$ that define the domain of an entire level $l = 0, \dots, l_{\max}$ by $G_l := \bigcup_{m=1}^{M_l} G_{l,m}$. Refinement grids are derived recursively from coarser ones and a hierarchy of successively embedded levels is thereby constructed, cf. Fig. 4. All mesh widths on level l are r_l -times finer than on level $l-1$, i.e. $\Delta t_l := \Delta t_{l-1}/r_l$ and $\Delta x_{n,l} := \Delta x_{n,l-1}/r_l$ with $r_l \in \mathbb{N}, r_l \geq 2$ for $l > 0$ and $r_0 = 1$, and a time-explicit FV scheme (in principle) remains stable under a condition like (15) on all levels of the hierarchy. The recursive integration order visualized in the left sketch of Fig. 5 is an important difference to usual unstructured adaptive strategies and is one of the main reasons for the high efficiency of the approach.

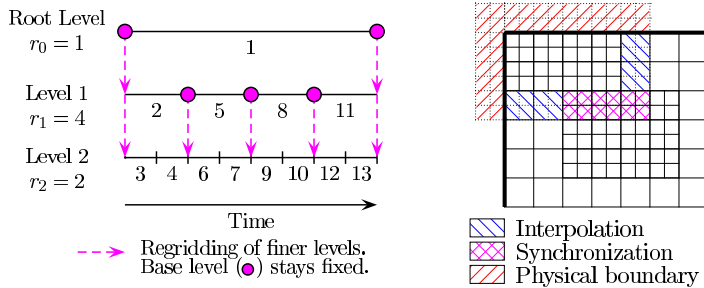


Fig. 5. Left: Recursive integration order. Right: Sources of ghost cell values.

The numerical scheme is applied on level l by calling the single-grid routines $\mathcal{H}^{(\Delta t)}$, $\mathcal{S}^{(\Delta t)}$ in a loop over all subgrids $G_{l,m}$. The execution of the numerical loop in `UpdateLevel()` in Alg. 2 requires the previous setting of the ghost cell values. Three types of boundary conditions have to be considered in the sequential case, see right sketch of Fig. 5. Cells outside of the root domain G_0 are used to implement physical boundary conditions. Ghost cells in G_l have a unique interior cell analogue and are set by copying the data value from the grid, where the interior cell is contained (synchronization). On the root level no further boundary conditions need to be considered, but for $l > 0$ also internal boundaries can occur. They are set by a conservative time-space interpolation from two previously calculated time steps of level $l - 1$.

Beside a general data tree that stores the topology of the hierarchy (cf. Fig. 4), the AMR method requires at most two regular arrays assigned to each subgrid which contain the discrete vector of state \mathbf{Q} for the actual and updated time step. In the Algorithms 2 and 3 we denote by $\mathbf{Q}^l(t)$ and $\mathbf{Q}^l(t + \Delta t_l)$ the unions of these arrays on level l . The regularity of the input data for the numerical routines allows high performance on vector and super-scalar processors and cache optimizations. Small data arrays are effectively avoided by leaving coarse level data structures untouched, when higher level grids are created. Values of cells covered by finer subgrids are overwritten by averaged fine grid values subsequently. The later operation leads to a modification of the numerical stencil on the coarse mesh and requires a special flux correction in cells abutting a fine grid. The correction replaces the coarse grid flux along the fine grid boundary by a sum of grid fluxes and ensures the discrete conservation property for the hierarchical method. See [2] or [5] for details.

The basic recursive AMR algorithm is formulated in Alg. 2. Except the regridding procedure, all operations have already been explained. New refinement grids on all higher levels are created by calling `Regrid()` from level l . Level l by itself is not modified. To consider the nesting of the level domains already in the grid generation, Alg. 3 starts at the highest refineable level l_c , where $0 \leq l_c < l_{\max}$. The refinement flags are stored in grid-based integer arrays N^l . A clustering algorithm [1] is necessary to create a new refinement

<pre> AdvanceLevel(l) Repeat r_l times Set ghost cells of $\mathbf{Q}^l(t)$ If time to regrid Regrid(l) UpdateLevel(l) If level $l+1$ exists Set ghost cells of $\mathbf{Q}^l(t + \Delta t_l)$ AdvanceLevel($l+1$) Average $\mathbf{Q}^{l+1}(t + \Delta t_l)$ onto $\mathbf{Q}^l(t + \Delta t_l)$ Correct $\mathbf{Q}^l(t + \Delta t_l)$ with $\delta \mathbf{F}^{n,l+1}$ $t := t + \Delta t_l$ </pre>	<pre> Regrid(l) For $\iota = l_c$ Downto l Do Flag N^ι according to $\mathbf{Q}^\iota(t)$ Generate $\check{G}_{\iota+1}$ from N^ι Ensure nesting of $\check{G}_{l+1}, \dots, \check{G}_{l_c+1}$ For $\iota = l+1$ To l_c+1 Do Create $\check{\mathbf{Q}}^\iota(t)$ from \check{G}_ι Interpolate $\mathbf{Q}^{\iota-1}(t)$ onto $\check{\mathbf{Q}}^\iota(t)$ Copy $\mathbf{Q}^\iota(t)$ onto $\check{\mathbf{Q}}^\iota(t)$ Set ghost cells of $\check{\mathbf{Q}}^\iota(t)$ $\mathbf{Q}^\iota(t) := \check{\mathbf{Q}}^\iota(t)$ </pre>
---	---

Alg. 2. Recursive AMR algorithm.**Alg. 3.** Regridding procedure.

$\check{G}_{\iota+1}$ on basis of N^ι until the ratio between flagged and all cells in every new grid $\check{G}_{\iota+1,m}$ is above a prescribed threshold $0 < \epsilon_{tol} < 1$.

The reinitialization of the hierarchical data structures is done in the second loop of Alg. 3 utilizing auxiliary data $\check{\mathbf{Q}}^\iota(t)$. Cells in newly refined regions $\check{G}_\iota \setminus G_\iota$ are initialized by interpolation, values of cells in $\check{G}_\iota \cap G_\iota$ are copied. As interpolation requires the previous synchronized reorganization of $\mathbf{Q}^{\iota-1}(t)$, recomposition starts on level $l+1$.

4.2 Parallelization

In the AMROC framework, we follow a rigorous domain decomposition approach and partition the AMR hierarchy from the root level on. We assume a parallel machine with P identical nodes and split the root domain G_0 into P non-overlapping portions G_0^p , $p = 1, \dots, P$ by

$$G_0 = \bigcup_{p=1}^P G_0^p \quad \text{with} \quad G_0^p \cap G_0^q = \emptyset \quad \text{for} \quad p \neq q.$$

The key idea now is that all higher level domains G_i are required to follow the decomposition of the root level, i.e.

$$G_i^p := G_i \cap G_0^p. \quad (17)$$

Condition (17) can cause the splitting of a subgrid $G_{l,m}$ into multiple subgrids on different processors. Under requirement (17) we estimate the work on an arbitrary subdomain $\Omega \subset G_0$ by

$$\mathcal{W}(\Omega) = \sum_{l=0}^{l_{\max}} \left[\mathcal{N}_l(G_l \cap \Omega) \prod_{\kappa=0}^l r_\kappa \right]. \quad (18)$$

Herein, $\mathcal{N}_l(\cdot)$ denotes the total number of FV cells on level l in the given domain. The product in (18) is used to consider the time step refinement.

A nearly equal distribution of the work necessitates

$$\mathcal{L}^p := \frac{P \cdot \mathcal{W}(G_0^p)}{\mathcal{W}(G_0)} \approx 1 \quad \text{for all } p = 1, \dots, P. \quad (19)$$

In AMROC, decompositions G_0^p with similar workload are found at runtime as the hierarchy evolves by a hierarchical partitioning algorithm based on a generalization of Hilbert's space-filling curve [25]. The space-filling curve defines an ordered sequence on the cells of the root level that can easily be split in load-balanced portions. As such curves are constructed recursively, they are locality-preserving and therefore avoid an excessive data redistribution overhead in the final loop of Alg. 3.

The second goal in designing an efficient parallelization strategy for distributed memory machines, the minimization of the communication costs, is already considered in condition (17) in a natural way. Together with the use of ghost cells this condition allows an almost local execution of Alg. 2. The only parallel operations that have to be incorporated are the parallel ghost cell synchronization and the application of flux correction terms across processor borders. See [5] for implementation details.

Analogous to Alg. 2 the regridding procedure of Alg. 3 is hardly affected by the parallelization as long as a repartitioning of the hierarchy is only allowed at root level time steps, which is usually sufficient in practice. New refinements $\check{G}_{\iota+1}^p$ can be found local, only a global concatenation of the new topology $\check{G}_{\iota+1} = \bigcup_p \check{G}_{\iota+1}^p$ is mandatory to ensure the correct proper nesting of the new hierarchy and to create a new load-balanced root level distribution G_0^p with the partitioner. Finally, the data distribution of parts of $\mathbf{Q}^t(t)$ to other processors must be incorporated.

5 Numerical Results

The self-sustaining CJ detonation of Sec. 3.5 is an ideal candidate for fundamental detonation structure simulations, because it produces extremely regular detonation cell patterns [29]. The application of the numerical methods of Sec. 3 within the parallel AMROC framework allowed a two-dimensional cellular structure simulation that is four-times higher resolved (44.8 Pts/ l_{ig}) than earlier calculations [24, 8, 11]. Only recently Hu et al. presented a similarly resolved calculation for the same CJ detonation on a uniform mesh [16]. Unfortunately, no technical details are reported for this simulation. In our case, the calculation ran on a small Beowulf-cluster of 7 Pentium III-850 MHz-CPU's connected with a 1 Gb-Myrinet network and required 2150 h CPU-time. On 24 Athlon-1.4 GHz double-processor nodes (2 Gb-Myrinet) of the HEidelberg LInux Cluster System (Helics) our approach allowed a sufficiently resolved computation of the three-dimensional cellular structure of a hydrogen-oxygen detonation. The maximal effective resolution of this calculation is 16.8 Pts/ l_{ig}

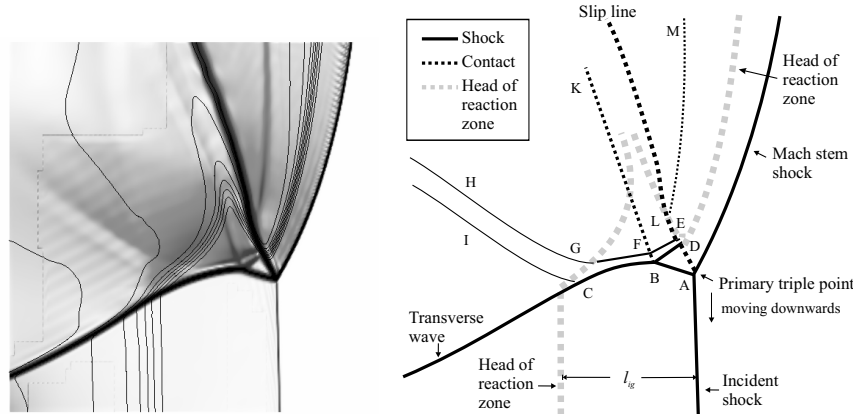


Fig. 6. Flow structure around a triple point before the next collision. Left: isolines of Y_{OH} (black) on schlieren plot of u_2 (gray).

and the run required 3800 h CPU-time. Our adaptive results are in perfect agreement with the calculations of Tsuboi et al. for the same configuration obtained on a uniform mesh on a super-scalar vector machine [33]. Further on, we present successful simulations of diffracting two-dimensional hydrogen-oxygen detonations that reproduce the experimentally measured critical tube diameter of 10 detonation cells. These computations demonstrate the advantages in employing a dynamically adaptive method impressively and used approximately 4600 h CPU-time on the Helics.

5.1 Two-dimensional Cellular Structure

We extend the one-dimensional ZND detonation of Fig. 3 to two space dimensions with $u_2 = 0$ and initiate transverse disturbances by placing a small rectangular unreacted pocket with the temperature 2086 K behind the detonation front, cf. [24] or [5]. After an initial period of $\approx 200 \mu\text{s}$ very regular detonation cells with $\lambda \approx 3 \text{ cm}$ and oscillation period $\approx 32 \mu\text{s}$ can be observed in computations with a resolution finer than $7 - 8 \text{ Pts}/l_{ig}$ (see [5] for a mesh refinement study). We exploit this regularity and simulate only a single cell. The calculation is done in a frame of reference attached to the detonation and requires just the computational domain $10 \text{ cm} \times 3 \text{ cm}$. The adaptive run uses a root level grid of 200×40 cells and two refinement levels with $r_{1,2} = 4$. A physically motivated combination of scaled gradients and heuristically estimated relative errors is applied as adaptation criteria. See [5] for details. Two typical snapshots with the corresponding refinement are displayed in Fig. 10. The adaptive computation uses between 340,000 and 390,000 FV cells, while a uniform grids with the same effective resolution would require 2,048,000 cells. About 3554 root level time steps ($C_{CFL} \approx 0.95$) to $t_{end} = 800 \mu\text{s}$ were calculated.

The high resolution of the simulation now admits a remarkable refinement of the triple point pattern introduced in Sec. 1. As the two transverse waves form a perfectly regular flow, it suffices to zoom into a single triple point and to analyze the wave pattern between two triple point collisions in detail. Fig. 6 displays the flow situation around the primary triple point A that is mostly preserved during the last $7\ \mu\text{s}$ before a collision. An analysis of the flow field uncovers the existence of two minor triple points B and C along the transverse wave downstream of A. While B can be clearly identified by a characteristic inflection, the triple point C is much weaker and very diffused. B is caused by the interaction of the strong shock wave BD with the transverse wave. The slip line emanating from B to K is clearly present. C seems to be caused by the reaction front (which can be interpreted as a diffused contact discontinuity) and generates the very weak shock wave CI. Downstream of BD a weaker shock wave EF shows up. It is refracted in the point F, when it hits the slip line BK. From F to G this minor shock is parallel and close to the transverse wave, what results in a higher pressure increase in the region FG than in the region EF. Unreacted gas crossing the transverse wave between B and C therefore shows a shorter induction length than gas entering through AB. The minor shock is refracted and weakened by the reaction front at point G and forms the shock GH that is almost parallel to CI. The downstream line of separation between particles passing through incident or Mach Stem shock is the slip line AD. Along its extension DEL the movement of A results in a shear flow between the reaction zones behind the Mach stem and downstream of BD.

In the actual picture the contact discontinuity LM seems to originate in this shear flow region, but a complete instationary analysis uncovers that it propagates constantly downstream. The collision of two triple points in the reinitiation of a detonation cell leads to the formation of an unreacted region behind the detonation front that burns in less than a microsecond. The burning generates upstream traveling shock waves that prevent the appearance of the flow field in Fig. 6 at an earlier stage. The strongest of these shocks hits the Mach stem from behind and forms an additional triple point with the contact discontinuity LM. In Fig. 6 shock and intermediate triple point have already vanished in A, but the contact discontinuity LM is still left behind. A detailed hydrodynamic analysis of the intermediate phase from reinitiation to the almost stable situation of Fig. 6 can be found in [5].

5.2 Three-dimensional Cellular Structure

We utilize the regular oscillating solution of the preceding section as initial condition for the three-dimensional simulation and disturb the oscillation in the x_2 -direction with an unreacted pocket in the orthogonal direction. We use a computational domain of the size $7\ \text{cm} \times 1.5\ \text{cm} \times 3\ \text{cm}$ that exploits the symmetry of the initial data in the x_2 -direction, but allows the development of a full detonation cell in the x_3 -direction. The AMROC computation uses a

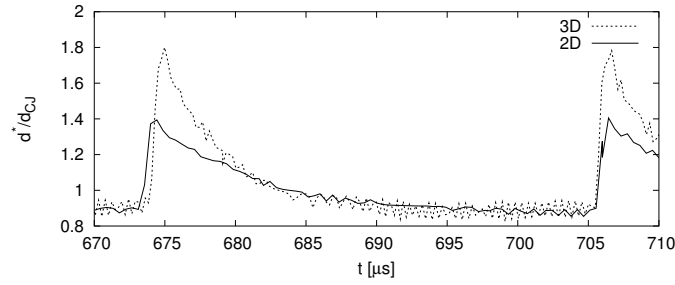


Fig. 7. Comparison of the temporal development of the detonation velocity along the line of symmetry through the middle of the detonation cells in the two- and three-dimensional simulation, cf. Figs. 10 and 11.

two-level refinement with $r_1 = 2$ and $r_2 = 3$ on a base grid of $140 \times 12 \times 24$ cells and utilizes between 1.3 M and 1.5 M cells, instead of 8.7 M cells like a uniformly refined grid (3431 root level time steps with $C_{CFL} \approx 0.95$ to $t_{end} = 800 \mu\text{s}$).

After a simulation time of $\approx 600 \mu\text{s}$ a regular cellular oscillation with identical strength in x_2 - and x_3 -direction can be observed. In both transverse directions the strong two-dimensional oscillations is present and forces the creation of rectangular detonation cells of 3 cm width. The transverse waves form triple point lines in three space-dimensions. During a complete detonation cell the four lines remain mostly parallel to the boundary and hardly disturb each other. The characteristic triple point pattern can therefore be observed in Fig. 11 in all planes perpendicular to a triple point line. Unlike Williams et al. [36] who presented a similar calculation for an overdriven detonation with simplified one-step reaction model, we notice no phase-shift between both transverse directions. In all our computations for the hydrogen-oxygen CJ detonation only this regular three-dimensional mode, called “rectangular-mode-in-phase” [14], or a purely two-dimensional mode with triple point lines just in x_2 - or x_3 -direction did occur.

A direct comparison of the temporal development of the detonation velocity in the two- and three-dimensional case in Fig. 7 along lines through the center of the graphics in Figs. 10 and 11 shows that both simulations reproduce the same oscillation period of approximately $32 \mu\text{s}$, but the detonation appears to be remarkably higher overdriven during reinitiation in the three-dimensional case.

5.3 Structure of Diffracting Detonations

Experiments have shown that the behavior of planar CJ detonations propagating out of tubes into unconfinement is determined mainly by the width of the tube. For square tubes the critical tube width has been found to be of the order of 10-times the cell width, i.e. 10λ [23]. For widths significantly below 10λ the process of shock wave diffraction causes a pressure decrease

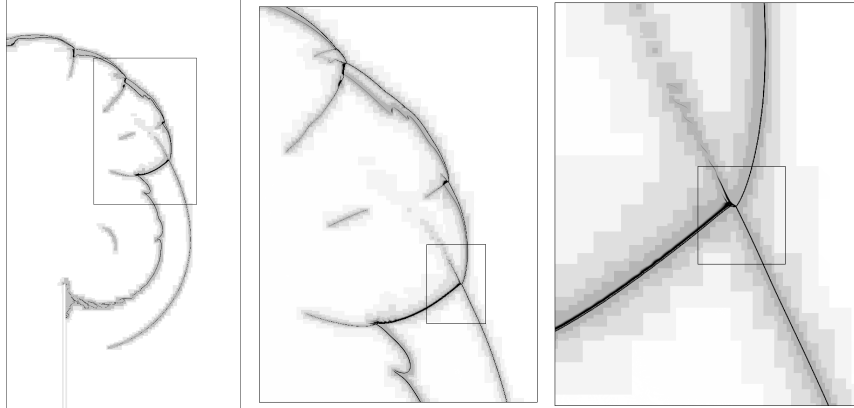


Fig. 8. Density distribution on four refinement levels at $t_{end} = 240 \mu s$ for $w = 10\lambda$.

at the head of the detonation wave below the limit of detonability across the entire tube width. Hydrodynamic shock and reaction front decouple and the detonation decays to a shock-induced flame. This observation is independent of a particular mixture. While the successful transmission of the detonation is hardly disturbed for tubes widths $\gg 10\lambda$, a backward-facing re-ignition wave reinitiates the detonation in the partially decoupled region for widths of $\approx 10\lambda$ and creates considerable vortices.

We are interested in the decoupling of shock and reaction and also in the re-ignition phenomenon. Therefore, we simulate the two-dimensional diffraction of the $H_2 : O_2 : Ar$ CJ detonation for the tube widths $w = 8\lambda$ and $w = 10\lambda$. A periodically reproduced snapshot of the regular oscillating detonation propagating into unreacted gas at rest is used as initial condition. This is a reasonable idealization for the flow situation in real detonation tubes directly before the experimental setup. The symmetry of the problem is exploited by simulating just one half.

The adaptive simulations utilize a base grid of 508×288 cells and use four levels of refinement with $r_{1,2,3} = 2$, $r_4 = 4$. The calculations correspond to a uniform computation with ≈ 150 M cells and have an effective resolution of 25.5 Pts/ l_{ig} in the x_1 -direction (with respect to the initial detonation). Both runs are stopped $240 \mu s$ after the detonation has left the tubes (730 root level time steps with $C_{CFL} \approx 0.8$), when the flow situations of interest are clearly established. The enormous efficiency of the refinement is visualized in Fig. 8 for the setup with $w = 10\lambda$. At t_{end} the calculation shown in Fig. 8 uses ≈ 3.0 M cells on all levels, where ≈ 2.4 M cells are inside one of the 2479 grids of the highest level ($\epsilon_{tol} = 0.8$).

A comparison of the flow fields in both setups after $240 \mu s$ in Fig. 9 clearly shows the extinction of the detonation for $w = 8\lambda$ and the re-ignition wave for $w = 10\lambda$. The reappearance of triple points at the detonation front in the

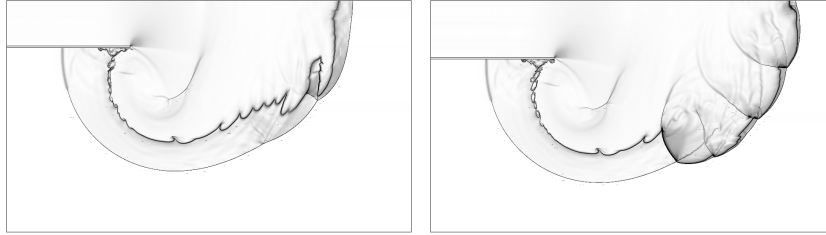


Fig. 9. Schlieren plots of ρ for a detonation diffracting out of the two different tubes. Left: detonation failure for the width $w = 8\lambda$, right: reinitiation for $w = 10\lambda$.

lower left plot in Fig. 9 is a characteristic indicator for the preservation of the detonation throughout the diffraction. It is interesting to note, that the re-ignition wave by itself is a detonation. The triple point track for $w = 10\lambda$ (not shown) uncovers that it has developed out of the transverse wave of an initial triple point.

6 Conclusions

We have described an efficient solution strategy for the numerical simulation of gaseous detonation waves with detailed chemical reaction. All temporal and spatial scales relevant for the complex process of detonation propagation were successfully resolved. The achieved resolutions are significantly finer than in earlier publications [24, 8, 11] and provide similar insight into the formation and propagation of transient detonation structures like recent large-scale simulations on uniform meshes [16, 33].

Beside the application of the time-operator splitting technique and the construction of a robust high-resolution shock capturing scheme, the key to the high efficiency of the presented simulations is the generic implementation of the blockstructured AMR method after Berger and Collela [2] in the AMROC framework [6]. AMROC provides the required high local resolution dynamically and follows a parallelization strategy that is tailored especially for the emerging generation of distributed memory architectures. All presented results have been achieved on Linux-Beowulf-clusters of moderate size in a few days real time, what demonstrates that advances in computational fluid dynamics do not necessarily require large super-computers, but integrated approaches, which combine fast and accurate discretizations with sophisticated techniques from computer science.

Acknowledgments

This work was supported by the DFG high priority research program “Analysis and Numerics of Conservation Laws”, grant Ba 840/3-3.

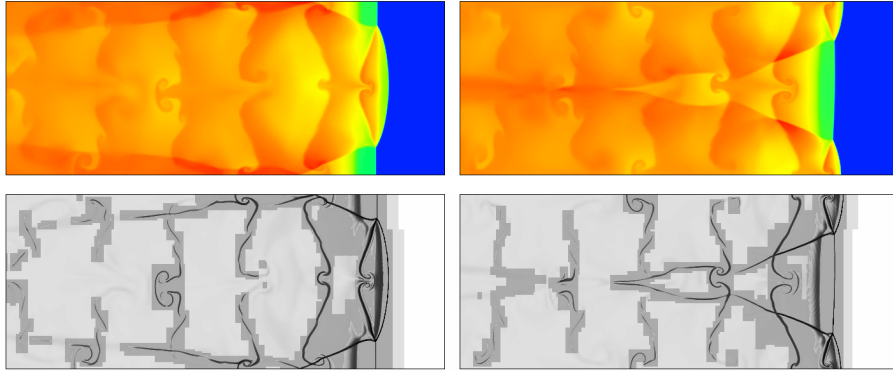


Fig. 10. Color plots of the temperature and schlieren plots of the density on refinement regions in the first (left) and second half (right) of a detonation cell.

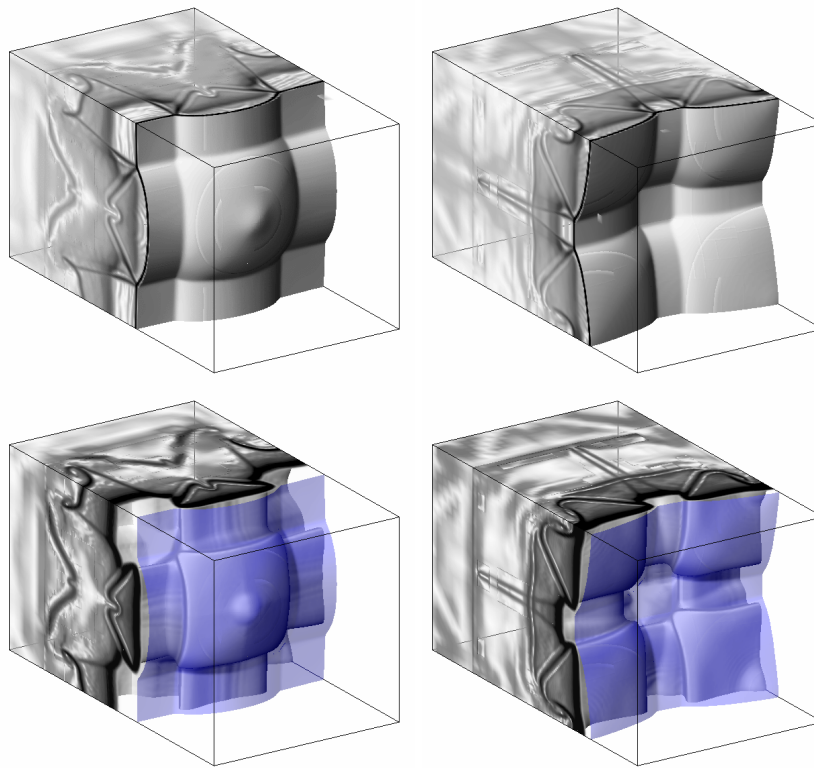


Fig. 11. Schlieren plots of ρ (upper row) and Y_{OH} (lower row) in the first (left) and second (right) half of detonation cell, mirrored at $x_2 = 0$ cm, $5.0 \text{ cm} < x_1 < 7.0$ cm. The plots of Y_{OH} are overlaid by a blue isosurface of ρ that visualizes l_{ig} .

References

- [1] J. Bell, M. Berger, J. Saltzman, and M. Welcome. Three-dimensional adaptive mesh refinement for hyperbolic conservation laws. *SIAM J. Sci. Comp.*, 15(1):127–138, 1994.
- [2] M. Berger and P. Colella. Local adaptive mesh refinement for shock hydrodynamics. *J. Comput. Phys.*, 82:64–84, 1988.
- [3] M. Berger and J. Olinger. Adaptive mesh refinement for hyperbolic partial differential equations. *J. Comput. Phys.*, 53:484–512, 1984.
- [4] R. Courant and K. O. Friedrichs. *Supersonic flow and shock waves*. Applied mathematical sciences, volume 21. Springer, New York, Berlin, 1976.
- [5] R. Deiterding. *Parallel adaptive simulation of multi-dimensional detonation structures*. PhD thesis, Brandenburgische Technische Universität Cottbus, Sep 2003.
- [6] R. Deiterding. AMROC - Blockstructured Adaptive Mesh Refinement in Object-oriented C++. Available at <http://amroc.sourceforge.net>, Mar 2004.
- [7] Y. N. Denisov and Y. K. Troshin. Structura gazovoi detonatsii v trubakh (Structure of gaseous detonations in tubes). *Zh. Eksp. Teor. Fiz.*, 30(4):450–459, 1960.
- [8] C. A. Eckett. *Numerical and analytical studies of the dynamics of gaseous detonations*. PhD thesis, California Institute of Technology, Pasadena, California, Sep 2001.
- [9] B. Einfeldt, C. D. Munz, P. L. Roe, and B. Sjögreen. On Godunov-type methods near low densities. *J. Comput. Phys.*, 92:273–295, 1991.
- [10] W. Fickett and W. C. Davis. *Detonation*. University of California Press, Berkeley and Los Angeles, California, 1979.
- [11] T. Geßner. *Dynamic mesh adaption for supersonic combustion waves modeled with detailed reaction mechanisms*. PhD thesis, Math. Fakultät, University Freiburg, 2001.
- [12] E. Godlewski and P.-A. Raviart. *Numerical approximation of hyperbolic systems of conservation laws*. Springer Verlag, New York, 1996.
- [13] B. Grossmann and P. Cinella. Flux-split algorithms for flows with non-equilibrium chemistry and vibrational relaxation. *J. Comput. Phys.*, 88:131–168, 1990.
- [14] M. Hanana, M. H. Lefebvre, and P. J. Van Tiggelen. Pressure profiles in detonation cells with rectangular or diagonal structure. In *Proc. of 17th Int. Colloquium on the Dynamics of Explosive and Reactive Systems*, Heidelberg, Jul 1999.
- [15] A. Harten. High resolution schemes for hyperbolic conservation laws. *J. Comput. Phys.*, 49:357–393, 1983.
- [16] X. Y. Hu, B. C. Khoo, D. L. Zhang, and Z. L. Jiang. The cellular structure of a two-dimensional H₂/O₂/Ar detonation wave. *Combustion Theory and Modelling*, 8:339–359, 2004.
- [17] N. N. Janenko. *Die Zwischenschrittmethode zur Lösung mehrdimensionaler Probleme der mathematischen Physik*. Springer-Verlag, Berlin, 1969.
- [18] P. Kaps and P. Rentrop. Generalized Runge-Kutta methods of order four with stepsize control for stiff ordinary differential equations. *Num. Math.*, 33:55–68, 1979.
- [19] R. J. Kee, F. M. Rupley, and J. A. Miller. *Chemkin-II: A Fortran chemical kinetics package for the analysis of gas-phase chemical kinetics*. SAND89-8009, Sandia National Laboratories, Livermore, California, Sep 1989.

- [20] R. J. Kee, F. M. Rupley, and J. A. Miller. *The Chemkin thermodynamic data base*. SAND87-8215B, Sandia National Laboratories, Livermore, California, Mar 1990.
- [21] B. Larrouturou. How to preserve the mass fractions positivity when computing compressible multi-component flows. *J. Comput. Phys.*, 95:59–84, 1991.
- [22] B. Larrouturou and L. Fezoui. On the equations of multi-component perfect or real gas inviscid flow. In Carasso et al., editor, *Proc. of Second Int. Conf. on Nonlinear Hyperbolic Equations - Theory, Numerical Methods, and Applications, Aachen 1988*, Lecture Notes in Mathematics 1402, pages 69–98. Springer-Verlag Berlin, 1989.
- [23] J. H. S. Lee. Dynamic parameters of gaseous detonations. *Ann. Rev. Fluid Mech.*, 16:311–336, 1984.
- [24] E. S. Oran, J. W. Weber, E. I. Stefaniw, M. H. Lefebvre, and J. D. Anderson. A numerical study of a two-dimensional H₂-O₂-Ar detonation using a detailed chemical reaction model. *J. Combust. Flame*, 113:147–163, 1998.
- [25] M. Parashar and J. C. Browne. On partitioning dynamic adaptive grid hierarchies. In *Proc. of the 29th Annual Hawaii Int. Conf. on System Sciences*, Jan 1996.
- [26] J. J. Quirk. Godunov-type schemes applied to detonation flows. In J. Buckmaster, editor, *Combustion in high-speed flows: Proc. Workshop on Combustion, Oct 12-14, 1992, Hampton*, pages 575–596, Dordrecht, 1994. Kluwer Acad. Publ.
- [27] R. Sanders, E. Morano, and M.-C. Druguet. Multidimensional dissipation for upwind schemes: Stability and applications to gas dynamics. *J. Comput. Phys.*, 145:511–537, 1998.
- [28] J. Smoller. *Shock waves and reaction-diffusion equations*. Springer-Verlag, New-York, 1982.
- [29] R. A. Strehlow. Gas phase detonations: Recent developments. *J. Combust. Flame*, 12(2):81–101, 1968.
- [30] R. A. Strehlow and F. D. Fernandez. Transverse waves in detonations. *J. Combust. Flame*, 9:109–119, 1965.
- [31] D. R. Stull and H. Prophet. JANAF thermodynamical tables. Technical report, U. S. Departement of Commerce, 1971.
- [32] E. F. Toro. *Riemann solvers and numerical methods for fluid dynamics*. Springer-Verlag, Berlin, Heidelberg, 2nd edition, 1999.
- [33] N. Tsuboi, S. Katoh, and A. K. Hayashi. Three-dimensional numerical simulation for hydrogen/air detonation: Rectangular and diagonal structures. In *Proc. of the Combustion Institute*, volume 29, pages 2783–2788, 2003.
- [34] B. van Leer. Towards the ultimate conservative difference scheme V. A second order sequel to Godunov’s method. *J. Comput. Phys.*, 32:101–136, 1979.
- [35] C. K. Westbrook. Chemical kinetics of hydrocarbon oxidation in gaseous detonations. *J. Combust. Flame*, 46:191–210, 1982.
- [36] D. N. Williams, L. Bauwens, and E. S. Oran. Detailed structure and propagation of three-dimensional detonations. In *Proc. of the Combustion Institute*, pages 2991–2998. 26, 1997.
- [37] F. A. Williams. *Combustion theory*. Addison-Wesley, Reading, Massachusetts, 1985.